



Topotactic synthesis of size-tuned MoS₂ inorganic fullerenes that allows revealing particular catalytic properties of curved basal planes



Pavel Afanasiev*

Institut de Recherches sur la Catalyse et l'Environnement de Lyon IRCELYON, UMR 5256, CNRS – Université Lyon 1, 2 av A. Einstein, 69626, Villeurbanne Cedex, France

ARTICLE INFO

Keywords:

Molybdenum disulfide
Inorganic fullerenes
Hydrogen evolution reaction
Thiophene HDS

ABSTRACT

Size-tuned hollow nanoparticles of MoS₂ sulfides (“inorganic fullerenes”, IF) have been prepared using topotactic solid-gas reaction of nanoparticulate scheelites AMoO₄ (A = Ca, Sr, Ba) with H₂S/CCl₄ mixtures in a wide range of temperatures. The hollow nanoparticles showed high specific surface areas and outstanding thermal stability. As shown by electron microscopy and Raman spectroscopy characterizations, the amounts of residual slabs edges and the curvature-related defects in the IF-MoS₂ particles can be controlled independently by means of varying the particle size and the preparation temperature. The slabs edges disappear when the temperature increases, whereas the curvature – related defects withstand thermal treatments but their amount depends of the particle size. Temperature programmed reduction suggested the presence of sulfur species with a decreased bonding energy, attributed to the slabs curvature. Catalytic tests in the electrochemical hydrogen evolution reaction (HER) and thiophene hydrodesulfurization (HDS) evidenced significant contribution of curved basal planes to the catalytic activity, the magnitude of the effect being size-dependent.

1. Introduction

Nanodispersed sulfides are widely studied as catalysts [1,2] lubricants [3], supercapacitors [4], photocatalysts [5] or electrodes in Li-ion batteries [6]. Layered MoS₂ and WS₂ sulfides are used as principal components of hydrotreating catalysts [7,8]. Recently they emerged as hydrogen evolution reaction (HER) electrocatalysts combining high activity and stability [9]. The edge sites of Mo(W)S₂ layers are known to be catalytically active in HER [10–12]. Much effort has been paid to engineer the morphology of Mo(W)S₂ materials to maximize the edges exposure [13–16] whereas basal planes are supposed to be catalytically inert [17]. However there is growing evidence in the literature of catalytic non-innocence of the basal planes. Thus, the defects of basal planes of the 2H-phase MoS₂ can exhibit excellent HER catalytic activity after resolving the problem of contact resistance between the catalyst and the support [18,19]. To activate basal planes one might consider bending them and creating strain, which would facilitate formation of defects. Strain can be applied to change electronic structure and concomitant optical properties in MoS₂ layers [20–22]. Chemical strain activation has been proposed to improve HER properties of MoS₂ [23].

Curved basal planes are exposed in the onion-like or hollow Mo(W)S₂ particles, also known as inorganic fullerenes (IF) [24]. Since their discovery by Tenne and coll. [25] many techniques were proposed for

IFs synthesis, including oxides sulfidation, [26] laser ablation [27], or metal-organic CVD [28]. Onion-like and hollow IF particles are studied for lithium batteries [29] lubricants [3] or shock absorbers [30]. However few studies exist of the catalytic properties of IFs as their closed shell structure exposes no edges. Earlier we demonstrated interesting catalytic properties of IF-MoS₂, suggesting non-negligible catalytic activity of curved and/or broken basal planes [31]. Still the role of curved and broken planes remains hypothetic. The main obstacle for the systematic study of slabs curvature effects was the absence of preparation techniques that would combine high yields with size tuning. IF materials prepared by the existing techniques often have wide size distributions and contain considerable impurities of non-IF morphologies. However to reliably identify the effects of curvature we need a series of pure IF materials with variable particle size.

This work describes a new preparation technique that affords size-tuned IF-MoS₂ materials in a wide temperature range. The feasibility of similar syntheses for IF-WS₂ has been also briefly demonstrated. The series of IF- MoS₂ materials were used to analyze the impact of slabs curvature on the electrocatalytic HER and in heterogeneous catalytic reaction of thiophene HDS.

* Corresponding author.

E-mail address: pavel.afanasiev@ircelyon.univ-lyon1.fr.

2. Experimental section

2.1. Preparation of scheelites precursors

Nanoparticles of Scheelites AMO_4 ($\text{M} = \text{Mo}, \text{W}$) were prepared by non-aqueous metathesis. All reactants were high purity grade from Aldrich. $\text{Ca}(\text{NO}_3)_2 \cdot 4\text{H}_2\text{O}$, $\text{Sr}(\text{NO}_3)_2$ or $\text{Ba}(\text{NO}_3)_2$ and $\text{Na}_2\text{MoO}_4 \cdot 2\text{H}_2\text{O}$ or $\text{Na}_2\text{WO}_4 \cdot 2\text{H}_2\text{O}$ were applied as precursors. Ethylene glycol, propylene glycol or formamide were used as solvents. Equimolar mixtures of two precursor salts (0.02 mol of each) were loaded in a flask containing 100 mL of a solvent. Then the mixtures were kept under 500 min⁻¹ stirring for 12 h. The obtained solids were separated by centrifugation, washed with the reaction solvent and with ethanol and dried at room temperature.

2.2. Preparation of hollow sulfides nanoparticles

The AMO_4 nanoparticles were converted to the mixtures of sulfides MS_2 ($\text{M} = \text{Mo}, \text{W}$) and chlorides ACl_2 ($\text{A} = \text{Ca}, \text{Sr}, \text{Ba}$) by means of reaction with the $\text{H}_2\text{S}-\text{CCl}_4-\text{Ar}$ gas mixture. A flow of Ar saturated with CCl_4 vapor at 0 °C was introduced using a glass saturator. The flow rates of H_2S and (CCl_4/N_2) were 30 mL/min and 10 mL/min, respectively. The solids (1–2 g) were treated in Pyrex (below 550 °C) or quartz (up to 750 °C) reactors. After the reaction the solids were washed several times with distilled water, separated and dried under nitrogen. The solids were handled and kept under inert atmosphere to avoid interaction with oxygen. The IF solids are designed according to the size of particles (nm) from which they have been prepared. Thus IF material obtained from 25 nm Scheelite of designed as Mo25 (or IF-Mo25). Bulk MoS_2 references were prepared using decomposition of ammonium thiomolybdate (ATM) under $\text{H}_2\text{S}/\text{H}_2$ flow in the range of temperatures 350–750 °C [32]. They are designed as ATM- MoS_2 (for series) or, for individual solids, just as MoS_2 according to the preparation temperature (e.g. MoS_2 -550 means the sample obtained from ATM at 550 °C under a flow of 10% $\text{H}_2\text{S}/\text{H}_2$).

2.3. Characterizations

Temperature-programmed reduction (TPR) was carried out in a quartz reactor. The samples of sulfides (0.01–0.015 g) were heated under H_2 flow (50 cm³.min⁻¹) from room temperature to 1050 °C at a rate 5 °min⁻¹. The H_2S and other gases produced in the reaction were detected by a Thermo Prolab quadrupole mass-spectrometer. Prior to the TPR measurement the samples were pre-treated in a flow of dry nitrogen at 100 °C.

Transmission electron microscopy (TEM) was carried out on a JEOL 2010 device with an accelerating voltage 200 keV. The samples were dispersed in ethanol by ultrasound, and then put onto a holey carbon filament on a copper grid sample holder. The analysis of images was carried out using Digital Micrograph Gatan™ software. Particle size was estimated from the analysis of low-resolution images, using ca. 200 particles for each solid.

The X-ray photoelectron spectroscopy (XPS) experiments were carried out on a KRATOS AXIS Ultra DLD spectrometer. The samples were pressed onto an indium foil, in a glove box under argon atmosphere. The spectra were acquired using monochromatic Al K α radiation (1486.6 eV, 150 W) and the binding energies (BE) were corrected taking C 1 s (284.6 eV) as the reference. Decomposition of the S 2p and Mo 3d XPS signals was carried out using the oxide and sulfide references. The effective atomic concentrations were corrected with respect to the sensitivity factors.

Raman spectra were recorded on a LabRam HR Raman spectrometer (Horiba-Jobin Yvon) equipped with a BXFM confocal microscope. The exciting line of an Ar⁺ ion laser at 514.5 nm was focused using a $\times 50$ objective. The backscattered light was dispersed with a grating of 1800 grooves mm⁻¹ providing a spectral resolution of 1 cm⁻¹. The position

of bands was calibrated from the 521 cm⁻¹ band of a Si plate.

Nitrogen adsorption isotherms were measured on a Micromeritics ASAP 2010 instrument. Specific surface area and pore size distribution were determined using BET and BJH equations, respectively. Prior to measurements, the samples were heated in a secondary vacuum at 350 °C for 4 h. The X-ray diffraction (XRD) patterns were obtained on a Bruker diffractometer with Cu-K α emission. Crystalline phases were identified using standard JCPDS files. Mean size of coherent scattering domains was determined using the Scherrer equation.

2.4. Thiophene HDS

Catalytic activity in thiophene hydrodesulfurization (HDS) reaction was measured at atmospheric pressure in a fixed-bed flow microreactor. Prior to catalytic tests, all samples were re-activated under the standard conditions by means of treatment under a flow of 10% $\text{H}_2\text{S}/\text{H}_2$ at 350 °C, for 2 h. Reaction was carried out in the temperature range 280–340 °C, under 50 mL/min gas flow, using 100–200 mg of catalyst and partial pressure of thiophene 2.7 kPa. The plug-flow reactor model was used to calculate the specific reaction rate, V_s , according to the equation

$$V_s = - (F/m) \ln(1 - x)$$

where F is the thiophene molar flow (mol/s), m is the catalyst mass (g), and x is thiophene conversion. Catalytic activity was estimated at steady state conversion, after at least 16 h on-stream. Arrhenius plots were built using four temperature points between 300 and 340 °C. High correlation coefficient (better than 0.995) and physically reasonable activation energy between 17 and 22 Kcal/mol were used as critetia of successful activity measurement. For each catalyst at least two HDS tests have been carried out.

2.5. Electrochemical measurements

To prepare the electrodes, 5 mg of a sulfide powder was dispersed by ultrasound in a solvent containing 800 μl of ethanol and 400 μl of 0.5% Nafion solution, optionally containing 1 mg of acetylene black carbon. Then 10 μl of suspension was dropped onto rotating glassy carbon electrode (0.0706 cm²) and dried in argon. The catalyst loading was about 0.6 mg/cm². The electrochemical measurements were performed on a VoltaLab three-electrode potentiostat using a Pt counter electrode and SCE reference at 25 °C in 0.1 M H_2SO_4 solution purged with bubbling argon. The LSV scans were obtained with iR compensation and scan rate 2 mV s⁻¹ in the potential range from 0.1 to –0.8 V vs. SCE. The initial 10–20 repeatable curves were used to characterize the materials. Electrochemical impedance spectroscopy (EIS) measurements were performed at different potentials with frequency from 0.01 Hz to 10 kHz and an amplitude of 5 mV in 0.5 M H_2SO_4 solution. To determine electrochemical surface area (ECSA), the same materials and the same loadings were applied as for HER study, but without carbon. The electrodes were studied in the double layer (non-Faradaic) region of CV, at different sweep rates (for details see SI).

3. Results and discussion

3.1. Solid-gas reaction mechanism and products

The synthetic approach combines two techniques described in earlier papers [33,34]. Non-aqueous blending of precursor salts affords nanoparticles (NP) of AMO_4 scheelites NPs ($\text{A} = \text{Ca}, \text{Ba}, \text{Sr}, \text{M} = \text{Mo}, \text{W}$) [33]. When carrying out precipitations in ethylene glycol or formamide, the size of obtained Scheelites particles depends on the nature of divalent cation and changed in the sequence $\text{Ba} > \text{Sr} > \text{Ca}$. On the other hand, for the same type of Scheelite, the particle size depends on the nature of non-aqueous solvent. Narrow size distributed

nanoparticles dispersions were obtained, due to ionic association and particular features of nucleation and growth, as discussed in [33]. Particle size and shape could be controlled in a wide range (5–300 nm) by varying the nature of the solvent and the precursor salts. Characterizations by powder XRD and TEM attest that pure Scheelite phases with narrow particle size distributions (PSD) were obtained (Fig. S1, S2).

On the second step of synthesis, the AMO_4 NP were transformed to hollow sulfides MS_2 under soft conditions by means of treating with a reactive gas mixture, containing CCl_4 vapor and H_2S . Carbon tetrachloride, as an oxophilic species, modifies the reactivity of oxides towards H_2S [34]. Solid-gas reactions of transition metals oxides with sole CCl_4 lead to the corresponding chlorides or oxychlorides [35,36]. Thus, above 300 °C CCl_4 transforms MoO_3 to volatile (oxy)chlorides that form yellow fuming deposits on the cold reactor outlet walls. If, however, an excess of H_2S is present in the gas flow, then $\text{Mo}(\text{W})$ sulfide is produced according to the Eq. (1).



For the reactions of AMO_4 precursors, introduction of CCl_4 in the gas mixture leads to a strong decrease of the free reaction energy, due to formation of CO_2 and electropositive chloride ACl_2 . As a result, the overall reactivity increases. Mass spectra of released gases confirm abundant production of CO_2 above 300 °C (Fig. S3a). Powder XRD patterns of non-washed samples show the presence of MS_2 and ACl_2 mixtures (Fig. S3b). Large ACl_2 particles were detected by TEM already at 350 °C (Fig. S3c). Without addition of CCl_4 the Scheelites react with H_2S , yielding soluble thiosalts below 400 °C or bulky reduced sulfide particles above 500 °C (Fig. S4).

Hollow sulfide particles obtained after washing replicate morphology of the AMO_4 precursors (Fig. 1). Therefore the solid-gas reaction is topotactic with respect to formed sulfide, but a simultaneous outburst of ACl_2 phase occurs. Hollow sulfide particles were obtained already at 350 °C for MoS_2 and above 400 °C for WS_2 . The NPs prepared above 400 °C contain mostly closed shells (> 90%) the rest being broken or opened particles. Therefore the release of ACl_2 crystals and the closure of MS_2 particles occur at relatively early reaction steps. Several works described genesis of IF particles due to an outburst of the interior, followed by formation of a closed shell structure. Thus, giant bubble mechanism proposed by Tremel et al., describes rupture of sulfide shells by the released gas [37]. Recently we obtained IF- MoS_2 from the $\text{MoS}_2@\text{ZnS}$ core-shell materials with an outburst of ZnS phase above 600 °C. Here large ACl_2 crystals are formed under much softer conditions (350–400 °C).

The XRD patterns after washing correspond to pure MS_2 phases, in a wide range of preparation temperatures (Fig. S5). TEM-EDS attest low contents of alkali earth metals (< 0.1% wt, Fig. S6).

The preparation method as described allows preparing gram quantities of hollow sulfides in laboratory. Beside isotropic IF solids versatile hollow morphologies (tubes, flowers, dendrites...) of sulfides at different size scales are available. Indeed, morphology-controlled syntheses of Scheelites are extensively studied due to their original physical properties. Microwave-assisted, non-aqueous or mixed-solvent precipitations were applied to obtain versatile objects of variable size [38–40]. Accordingly, new possibilities are opened for the morphology-controlled synthesis of the corresponding sulfides. Thus, spindle-like hollow microparticles of WS_2 were obtained from BaWO_4 spindles (Fig. 1f, Fig. S1d). Molybdates and tungstates react similarly, though tungstates show slightly lower reactivity. In the following sections we focus on the properties of IF- MoS_2 solids as a function of the precursor morphology and preparation temperature.

3.2. Morphology of the IF- MoS_2 particles

For the systematic study, four molybdenum-containing solids were

selected, with variable mean particle radius of precursor: CaMoO_4 of 18 nm, SrMoO_4 of 24 and 35 nm and BaMoO_4 of 71 nm size, respectively. The IF- MoS_2 NPs derived from these precursors were studied as concerns their particle size, walls thickness and MoS_2 slabs morphology. The properties of materials prepared at 450, 550, 650 and 750 °C are discussed (for thiophene HDS preparation at 350 °C was also included in the series). The samples are designated according to the mean particle size of precursor and the treatment temperature. Thus Mo24-550 designates a MoS_2 material prepared at 550 °C from a Scheelite (SrMoO_4) NPs with a mean particle radius 24 nm.

3.2.1. Particle size

The IF- MoS_2 NPs size and particle size distribution (PSD) are similar to those of the AMO_4 precursors whatever the preparation temperature (Fig. 1f, Fig. S7, Table S1.). Therefore no significant coalescence or ripening of NPs occurred. However for the Mo35 and Mo71 solids, the sulfide particles are slightly larger than the initial AMO_4 (Fig. 1f). Therefore outward diffusion of the Mo species (Kirkendall mechanism) and/or NPs dilatation by released gases partially contribute to the morphology genesis.

The possibility to transform AMO_4 particles to the single (one void, one shell) objects appears limited for both too small and too large sizes. Though AMO_4 NPs of size down to 5 nm are available [33], the NPs with a radius lesser than 10 nm do not undergo exact replication, but hollow agglomerates are formed (Fig. S8a). For the AMO_4 NPs larger than 150 nm, multiple voids appear and porous NPs are formed, with an exterior shape replicating that of the precursor particle (Fig. S8b). For large particles, nested structures were also observed, containing planar 2D sheets inside the IF, as described for IF- WS_2 grown in the presence of iodine [41].

3.2.2. MoS_2 hollow spheres wall thickness and textural properties

Morphology of sulfide slabs and their packing are the major parameters defining the textural properties. Hollow particles are formed because the molar volume of MoS_2 product is lesser than the molar volume of AMoO_4 precursor (Table S2). Beside molar volumes, the wall thickness depends on the initial AMoO_4 NP size and on the solid-gas reaction mechanism, inward or outward.

If diffusion of reacting species from gas into the solid (e.g. sulfur species in an oxide framework) is a rapid step, then the reaction front propagates from the surface into the particle volume and inward mechanism takes place. Otherwise, if penetration of the gas reactant species into the solid is difficult, but the species of the solid reactant have mobility sufficient to pass through the solid product shell and react at the surface, then outward (Kirkendall type) mechanism is observed. For the initial AMoO_4 spheres of a radius R_0 the product MoS_2 hollow spheres will have inner radius R_1 and outer radius R_2 , depending on the mechanism. For the inward reaction propagation $R_2 = R_0$ and for an outward process $R_1 = R_0$. The walls should be relatively thicker and the specific surface areas lower for the inward mechanism. Wall thickness and specific surface areas calculated for pure inward and outward mechanisms are shown by dashed lines in Fig. 2a, b. The experimental values agree with the inward mechanism at lower R_0 , but deviate towards thinner walls for higher R_0 (Fig. 2a), confirming involvement of the outward mechanism.

If TEM observation gives the wall thickness of a layer of solid matter independent on its inner structure, the wall thickness determined from the MoS_2 phase XRD (002) line broadening characterizes the mean stacking of crystalline slabs. The XRD thickness is always lesser than TEM thickness, in particular if the walls are loosely packed. The observed XRD wall thickness expectedly increases with the preparation temperature, but remains smaller than the TEM-derived wall thickness, probably owing to a persistent disorder of slabs packing (Fig. 2c). At low temperatures the slabs stacking seems to be similar for all samples. At higher temperatures the average slabs stacking becomes size-dependent: the larger the particle size, the greater the slabs stacking

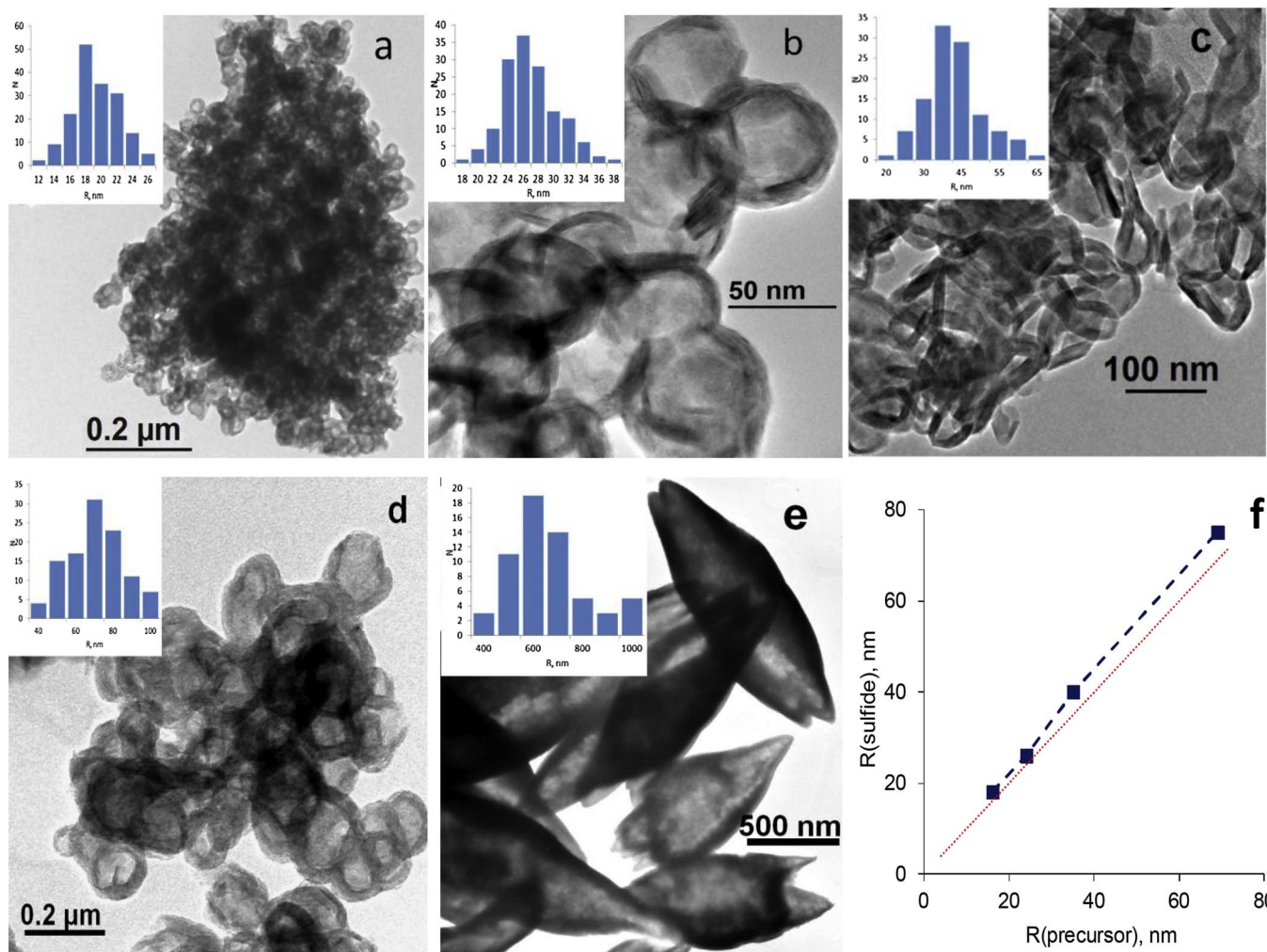


Fig. 1. TEM images of selected hollow sulfides: (a) Mo18-550; (b) Mo24-450; (c) Mo35-750; (d) Mo71-550; (e) W1200-650; (f) sulfide particle size vs. precursor particle size for the samples obtained at 550 °C. Insets in (a–e) – particle size histograms.

(Fig. 2c). The increase of slabs stacking with temperature is restrained in the IF-MoS₂ solids, as compared with the ATM-MoS₂ reference (Fig. 2c), i.e. the inorganic fullerenes are more stable to sintering.

Nitrogen adsorption measurements show specific surface areas and thermal stability outstandingly high for this type of materials. Thus, for the Mo18 series S_{sp} only decreased from 110 to 87 m²/g when the preparation temperature increased from 450 to 750 °C (Fig. 2b). The specific surface areas of larger particles (Mo71) remain greater than predicted by geometric model (Fig. 2b). Indeed, overall TEM morphology is not appropriate to calculate specific surface area, because the walls possess inner porosity. This inner porosity contributes to the BET surface area, making it greater than TEM geometry –derived value.

Pore size distributions and N₂ adsorption hysteresis loops for IF-MoS₂ reveal predominance of large pores (meso and macropores) and limited amount of micropores. The mean pore size varied in step with the size of IF particles (Fig. 2d). As the temperature increases, volume of micropores decreases, due to ordering of the slabs packing (Fig. 2e, f).

3.2.3. Morphology of slabs

High resolution TEM provides the details of MoS₂ slabs morphology (Fig. 3). The solids obtained below 400 °C are relatively disordered (not shown). Beginning from 450 °C, hollow particles with concentric sulfide slabs were obtained as a major product, in agreement with earlier results by Zink et al. who observed tangential orientation of slabs between 400 and 600 °C in the onion-like MoS₂ and WS₂ [42]. However, while

having overall tangential directionality of slabs, the materials obtained at 450 and 550 °C contain many defects (Fig. 3a, b). With the increase of preparation temperature the amount of defects decreases (Fig. 3c, e, g, h).

The main type of defects in the walls interior is the step dislocations in the (002) planes (Fig. 3d). Step dislocations were observed earlier in hollow IF-MoS₂ and their presence arguably contributes to bending of the IF walls [43]. A dislocation in the interior of a wall usually gives rise to a breaking line on the surface, in the vicinity of that dislocation (Fig. 3d). While being 1D surface defects, such breaking lines are obviously distinct from the free (dangling) edges. Beside dislocations, some steps (residual edges) remain on the surface even after prolonged heating at 750 °C (Fig. 3i).

Both broken and curved slabs are present in all solids, whatever the particle size and the temperature. High temperature favors broken slabs (Fig. 2c, e, g), whereas at moderate temperatures uniformly curved planes dominate (Fig. 2a, b, f). Morphology evolution upon increase of temperature could be visualized as crystallization of polyhedral shapes. However, the versatility of defects and uncertainty of their representation in the conventional TEM make difficult quantification of these features. Quantification of these morphologies might probably be achieved by means of 3D microscopy, which proved to be eminently useful for accessing fine morphology details in sulfide catalysts [44].

Defects and slabs curvature are interrelated and dynamic equilibrium exists between them. The ability of graphene-like sheets to buckle when defects are introduced plays an important role in the strain

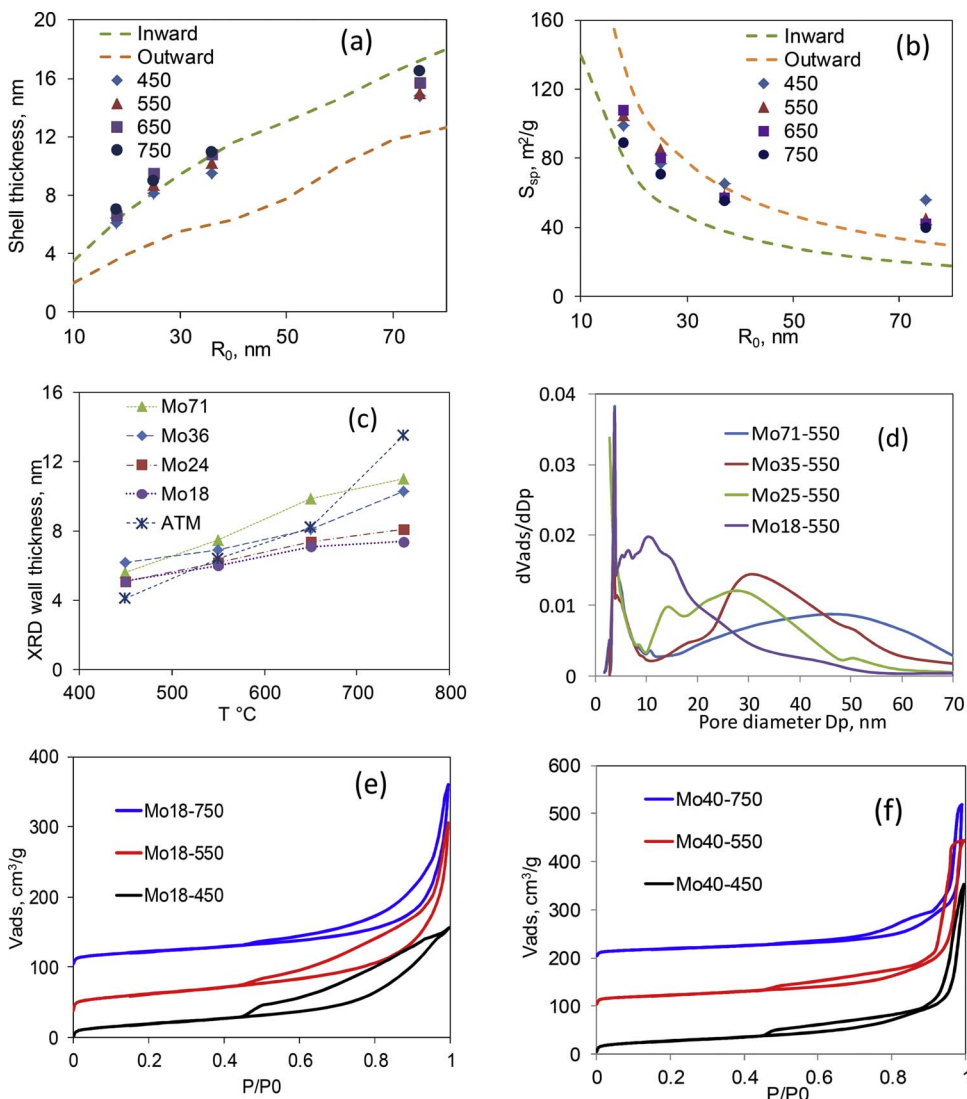


Fig. 2. TEM wall thickness (a) and specific surface area (b) of IF-MoS₂ solids as a function of precursor particle radius. Dashed lines show the calculated values for inward and outward reaction propagation, respectively, taking into account unequal molar volumes of different precursors; (c) XRD wall thickness vs. preparation temperature for IF-MoS₂ solids and ATM reference; (d) pore size volume distribution for IF-MoS₂ solids prepared at 550 °C; nitrogen adsorption isotherms of selected samples from Mo18 (e) and Mo35 (f) series.

relief [45]. Inversely, in the buckled sheets, an increased amount of defects is expected. The broken slabs as seen in the 2D TEM correspond in the real 3D particles to some linear defects. The preferred structure of such linear defects is yet unclear, but is actively investigated. In the monolayer MoS₂, grain boundaries consisting of 5- and 7- member rings were directly observed [46]. Intrinsic defects present in the MoS₂ layers include vacancies, antisite defects and versatile grain boundary structures, some of which show metallic behavior [47]. In the grain boundaries, antisites are supposed to dominate and more than one hundred physically reasonable interface structures of this type have been constructed [48].

In summary, hollow IF-MoS₂ NPs were obtained with variable particle size, narrow PSDs and controlled walls defectness. The preparation temperature does not significantly affect the particle size. At the same time the slabs morphology depends on the preparation temperature. In the following sections we compare the properties of these solids to unravel the impact of slabs curvature.

3.3. Raman spectroscopy

Raman spectroscopy has been widely applied to characterize MoS₂ thin films and nanoparticles because the main Raman features are affected by the number of layers in the stacks, the strain in the layers and the defects of MoS₂ particles. Two main lines in the Raman spectra of MoS₂ corresponding to the A_{1g} and E_{2g}¹ modes and the weaker E_{1g}

mode were observed respectively at 403–408 cm⁻¹, 379–382 cm⁻¹ and 286 cm⁻¹ (Fig. 4a). For thin MoS₂ films from monolayer to 5–6 slabs, the main A_{1g} and E_{2g}¹ lines change their position, moving farther apart as the stacking number increases [49,50]. However since the IF-MoS₂ samples at stake have the walls thickness above 6–8 slabs, the difference of A_{1g} and E_{2g}¹ frequencies varies weakly, being close to the bulk values (Fig. 4a). Similar results on larger IF-MoS₂ were obtained earlier [51]. Nevertheless, for the low-temperature preparations (450 °C, whatever the particle size) considerable lines broadening occurred, with a slight variation of A_{1g} – E_{2g}¹ frequency difference between 24 and 26 cm⁻¹. Probably, due to disorder, the effective slabs stacking is smaller when the preparation temperature is lower.

Besides the two main modes, for small and/or disordered MoS₂ particles additional peaks appear corresponding to zone-edge phonons [52]. When the ($q = 0$) selection rule is relaxed, new modes are observed among which the most intense longitudinal acoustic mode at M point LA(M) is located at 226–227 cm⁻¹. This mode observed in MoS₂ nanoparticles has been attributed to the defect-induced scattering, as its intensity was found to be proportional to the density of defects [53,54], whereas it is absent in the good quality crystals [55]. The LA(M) mode appears to be diagnostic for the defectness of the IF-MoS₂ systems under study. Its intensity changes with both the particle size and the preparation temperature. The vibration LA(M) at 227 cm⁻¹ is not specific for the IF structure and is observed also in the ATM-MoS₂. In both ATM-MoS₂ and IF-MoS₂ the relative intensity of the LA(M) mode decreases

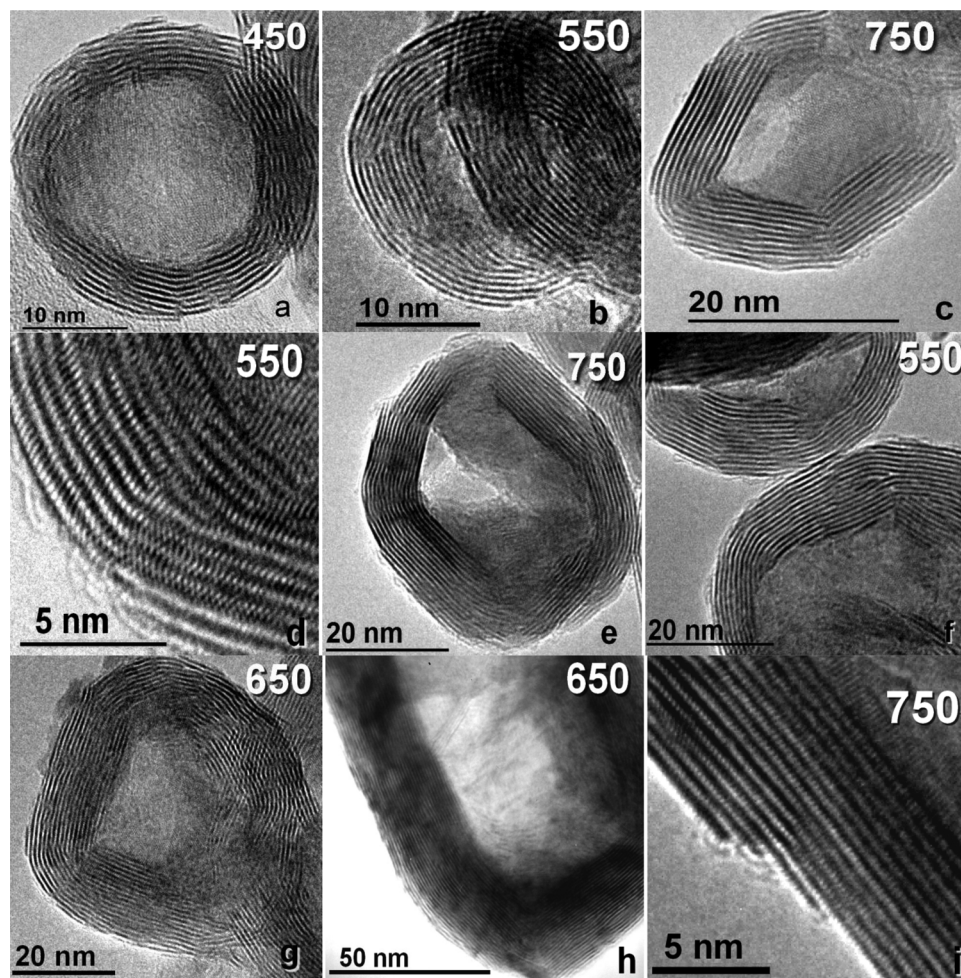


Fig. 3. HRTEM images of Mo18 (a-c), Mo24 (d, e) Mo35 (f, g) and Mo71 (h, i). The solid at image (i) was heated for 12 h, for the rest the treatment time was 4 h.

with the preparation temperature, as the defects are annealed. The size dependence of LA(M) intensity is not manifested for low preparation temperatures but becomes obvious at 750 °C, with smaller particles having larger amount of defects. Thus both large Mo71 particles and ATM show almost total disappearance of the LA(M) band after treatment at 750 °C, whereas small Mo18 and Mo24 retain considerable amount of defects. Worth emphasizing that the LA(M) intensity is not correlated to the specific surface area. The latter changes only slightly upon annealing of IF-MoS₂ solids and strongly for ATM, whereas the LA(M) band varies strongly in all cases.

3.4. Temperature programmed reduction (TPR)

TPR has been applied to access the speciation of sulfur subsequently removed from MoS₂ by hydrogen upon progressive heating. The TPR patterns of bulk MoS₂ show a low-temperature peak (150–250 °C) due to reduction of the S₂²⁻ edge moieties, followed by an ill-defined intermediate zone (300–600 °C) and an exponentially ascending branch above 700 °C due to quasi-equilibrium bulk reduction [56].

Here TPR is applied to identify sulfur species related to the presence of bent and/or broken slabs that should probably have weaker Mo-S bonding and be easier reducible than basal planes in the reference ATM-MoS₂. Moreover, the slabs edges are quantified by integrating the low-temperature peak. In the closed-shell IF – MoS₂ NPs the amount of exposed edges is supposed to be lower than in a non-IF bulk MoS₂. Since the edges strongly influence the catalytic properties, their quantification is crucial for accessing the morphology-activity relationship. Relative area of the first TPR peak of IF-MoS₂ decreases with the preparation temperature (Fig. 5a) in agreement with earlier work on ATM-

MoS₂ [57]. In both IF- and ATM-MoS₂ the edges progressively disappear at higher preparation temperatures. The area of the first TPR peak is expectedly lower in the IF-MoS₂ than in ATM-MoS₂ prepared at the same temperature (Fig. 5c). A notable difference was observed between the high temperature parts of TPR curves for IF- and ATM-MoS₂. For ATM-MoS₂ the ascending part of TPR curves obeys the Vant Hoff equation [34]. By contrast, for the IF-MoS₂ an additional intensity in the range 750–900 °C was observed (Fig. 5b). We tentatively attribute this feature to the sulfur species from bent and/or broken slabs. As follows from TPR, sulfur bonding is such species is much stronger than in the S₂²⁻ moieties at the edges, but lower than in the bulk MoS₂. Since this TPR intensity is smeared over the main ascending TPR branch, its integration has a high uncertainty (at least 30% relative error). However a rough estimate confirms the expected size dependence: smaller particles show greater “curvature-related” TPR intensity (Fig. 4d). For the smallest particles of Mo18 series, the amount of such curvature-modified sulfur species corresponds to approximately 1.5–2% of total sulfur.

As the amount of S atoms with curvature-modified properties seems not to exceed few percent, physical methods probing the totality of bulk or surface Mo and S atoms are not appropriate. Thus, the XPS technique appears not diagnostic. The Mo 3d and S 2p XPS signals are similar in the IF- and ATM-MoS₂ solids (Fig. 6, S9). Indeed, even if modified S and Mo species do exist, the difference of BE is presumably moderate and such minority species should not be distinguishable from the overlapping strong signal from regular MoS₂.

Overall, the data on morphology, Raman spectra and TPR curves evidence that in the series of IF-MoS₂ solids the particle size and the relative amount of edges can be controlled independently. The amount

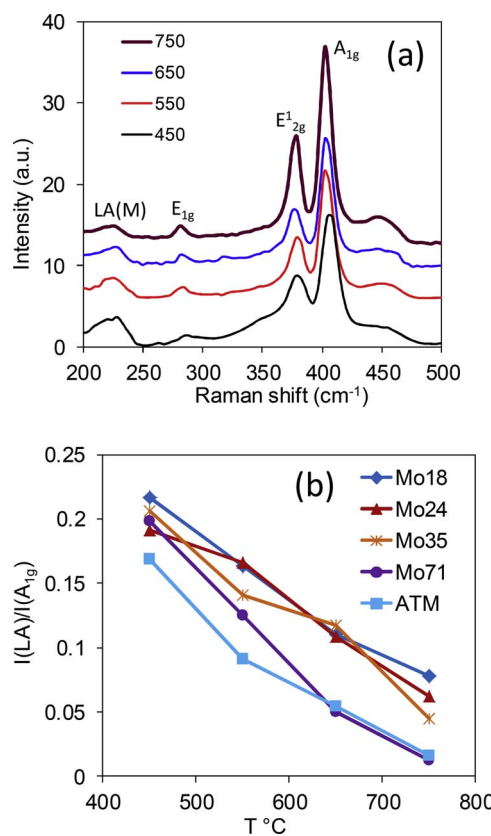


Fig. 4. Raman spectra of Mo18 IF-MoS₂ sample vs. treatment temperature (a) and the intensity of defect-related line LA(M) for the IF-MoS₂ series and ATM reference as a function of preparation temperature (b).

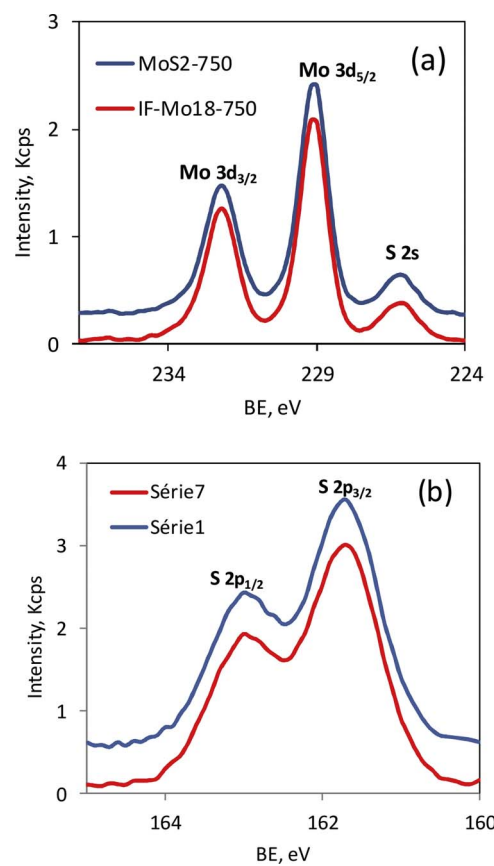


Fig. 6. Mo 3d (a) and S 2p (b) XPS spectra of IF-MoS₂ and non-fullerene MoS₂ treated at the same temperature 750 °C.

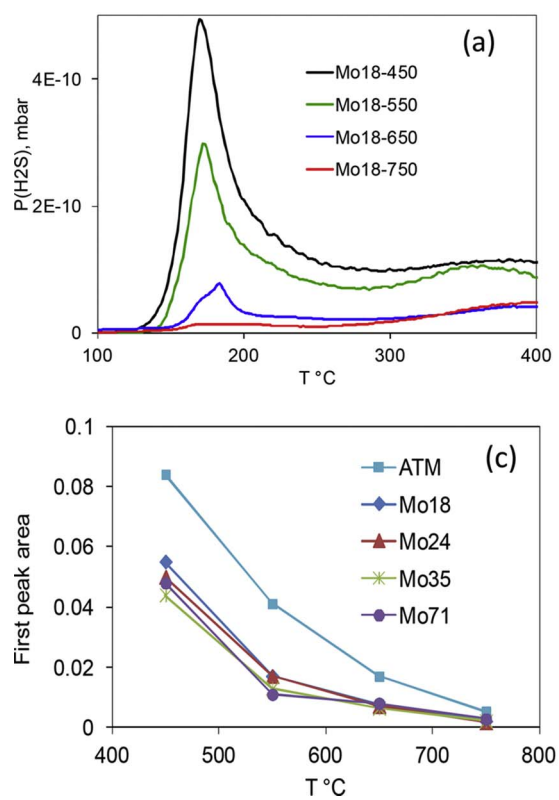


Fig. 5. (a) Low-temperature TPR peak vs. preparation temperature, as exemplified by Mo18; (b) additional TPR intensity for the IF-MoS₂ of different size prepared at 550 °C; (c) relative amounts of edges in the IF-MoS₂ materials and ATM-MoS₂; (d) relative amounts of curvature-modified sulfur species in the IF-MoS₂ of different size vs. preparation temperature.

of edges depends mostly on the treatment temperature while the particle size remains nearly constant. That allows probing curvature-related effects on the catalytic properties, as follows.

3.5. Electrochemical HER

Though the ability of MoS_2 to be a HER catalyst was discovered decades ago [58], many recent works report on versatile ways to MoS_2 -based and similar WS_2 -based HER electrodes on different supports [9–17]. The role of the contact between MoS_2 and its support has yet to be fully understood, but obviously the morphology and the directionality of MoS_2 on the support and chemical nature of the contact are crucial, as well as interfacial band bending. Here the goal is to investigate specific effects brought by the IF- MoS_2 structure in a series of electrodes prepared by a simple and well-benchmarked method. Few works have been carried out so far on the IF- MoS_2 materials, because improving the MoS_2 slabs design to maximize the number of edges has been the main research focus. Several earlier works on electrochemical HER using monometallic and Re-doped IF- MoS_2 suggest that the IF structure is favorable for HER [59–61]. Improved electrochemical performance of monolayer MoS_2 supported on porous gold was attributed to the MoS_2 slabs curvature [62].

Electrocatalytic HER activity was studied by linear sweep voltammetry (LSV) and HER kinetics was evaluated using the Tafel equation ($\eta = b \log J + a$, where η is the overpotential, J is the current density, and b is the Tafel slope).

The electrochemical surface areas of selected samples as determined from the variable rate CV in the double layer (non-faradaic) region of potentials appear to be lower than the BET surface areas (Table S3, Fig. S10). This difference is probably due to incomplete penetration of electrolyte inside the smallest pores and/or clogging of some pores with Nafion. This effect is more pronounced for the samples treated at 450 °C than for 750 °C counterparts, due to higher amount of micropores in the formers.

The values of the 10 mA/cm² overpotentials (η_{10}) and Tafel slopes (Ts) are given in Table S1. For the IF- and ATM-derived MoS_2 obtained at low temperature (450 °C) the Ts values are similar, whereas the currents are slightly higher for the IF- MoS_2 solids (Fig. 7a, b, Table S1). However as the preparation temperature increases, the figures of HER performance diverge in favor of the IF- MoS_2 . For MoS_2 -750, Ts increases to 205 mV/decade whereas for the IF- MoS_2 it remains in the range 100–120 mV/decade (Fig. 7a, b).

Deactivation of ATM-derived samples with the preparation temperature occurs due to the disappearance of slabs edges. According to TPR, MoS_2 -750 sample and IF- MoS_2 -750 series (of different size) contain very small amounts of exposed edges (Fig. 5c). By contrast, IF- MoS_2 -750 samples demonstrate HER activity still comparable to that of the low-temperature preparations (Fig. 7c). The current densities for the IF- MoS_2 -750 series are an order of magnitude greater than for the non-IF counterpart, in agreement with previous results by Chhetri et al. [38,39]. Therefore the curved and/or broken slabs of IF- MoS_2 are responsible for a substantial HER activity. The effect is size-dependent. While Tafel slopes are close, the currents are higher for the systems with smaller particles (Table S1).

Electrochemical impedance spectroscopy (EIS) measurements were used to further characterize the electrode kinetics for HER. The impedance spectra were fitted with an equivalent circuit model containing a solution resistance R_s , a charge transfer resistance R_{ct} and a constant phase element CPE. Fig. 7d shows the complex plane Nyquist plots for MoS_2 -750 and a series of IF- MoS_2 -750 solids of different size. The radius of Z' - Z'' semicircle is smaller for the IF- MoS_2 of smaller particle size, implying more efficient electron transfer at the interface between the surface of IF- MoS_2 and electrolyte. The reaction resistance (R_{ct}) for MoS_2 -750 is 3500 Ω, whereas from Mo71-750 to Mo18-750, it decreased from 1620 to 870 Ω respectively (the R_s values are small and non-specific for the solids studied). Therefore IF- MoS_2 structure favors

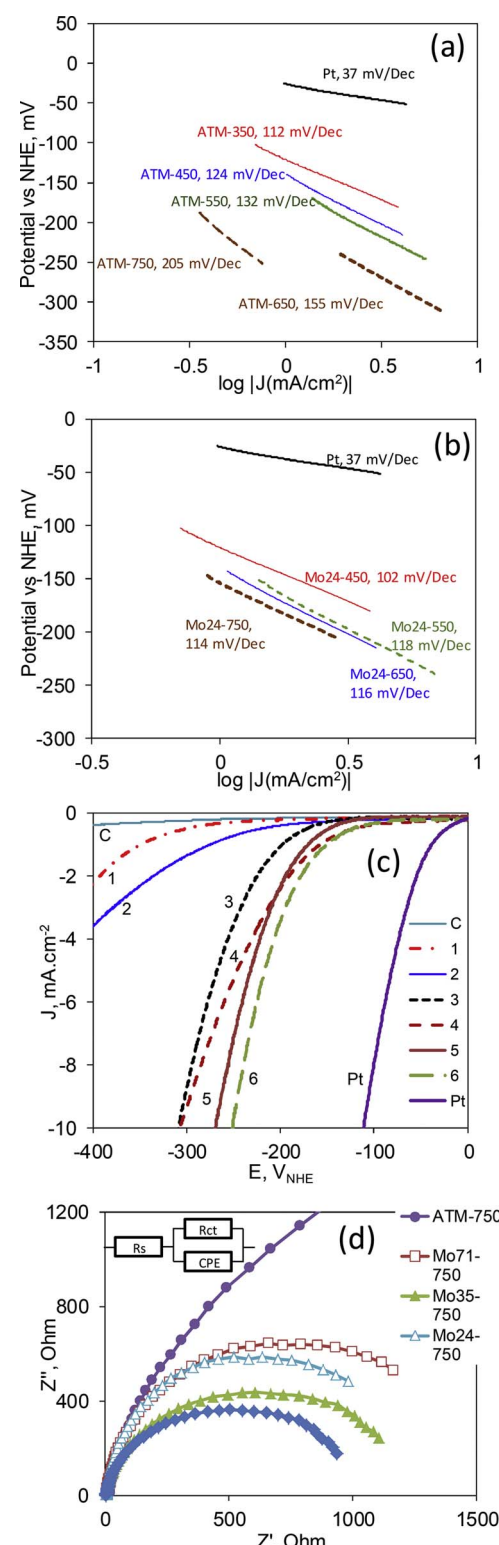


Fig. 7. Electrochemical HER measurements in 0.5 M H_2SO_4 electrolyte. Tafel plots for ATM-derived (a) and Mo24 series (b) vs. treatment temperature. (c) LSV curves for 1- MoS_2 -750, 2- MoS_2 -650, 3- MoS_2 -450, 4- MoS_2 -450, 5- MoS_2 -550 and 6- MoS_2 -450. (d) electrochemical impedance spectra (EIS) at an overpotential –200 mV vs RHE.

the efficient charge flow from the electrode to the surface active sites of the sulfide NP.

Besides the obvious explanation by weakening of sulfur bonding and formation of active defects, other plausible mechanisms of HER activity increase could be proposed. Metallic conductivity could appear near the

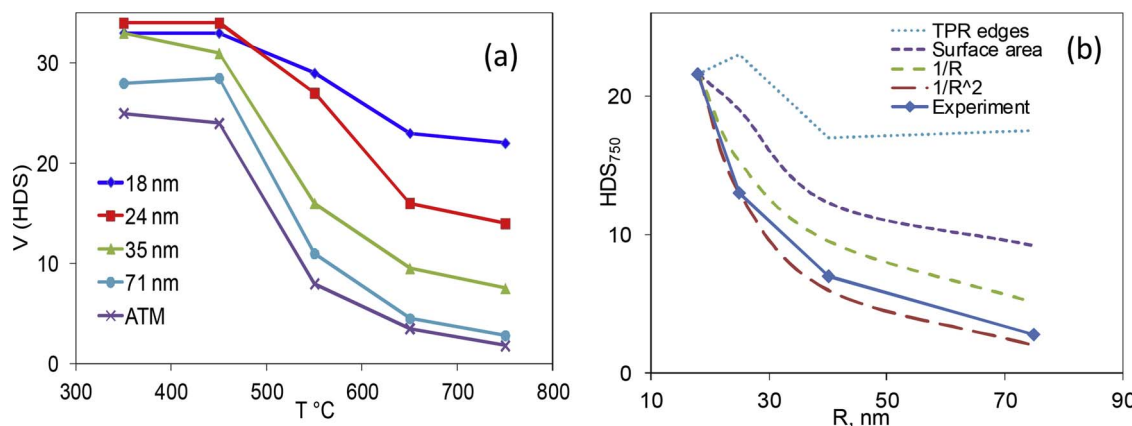


Fig. 8. (a) Thiophene HDS rate at 300 °C ($\text{mol g}^{-1}\text{s}^{-1} \cdot 10^{-8}$) as a function of preparation temperature for IF-MoS₂ series and MoS₂ from ATM decomposition reference. (b) HDS₇₅₀ rate as a function of particle size, compared with (normalized) variations of inverse powers of size, specific surface area and TPR-determined amount of edges.

breaking lines or in the zones of strong curvature. Theory works by Enyashin and coll. show that metallic character can be acquired in hollow octahedral molybdenum sulfide fullerenes, due to a nearly vanishing gap between the HOMO and the LUMO [63].

3.6. Thiophene HDS

Thiophene hydrodesulfurization (HDS) catalytic test allows evaluating the potential of IF-MoS₂ materials as hydrotreating catalysts and reveals the relationship between morphology and activity. In Fig. 8 are shown the steady-state thiophene HDS conversion rates as a function of treatment temperature for the IF solids and ATM-MoS₂ reference. For all catalysts thiophene HDS activation energy was in the range of 85–95 kJ mol⁻¹ in agreement with previous studies [64,65].

The specific HDS rate varies as a function of both particle size and preparation temperature (Fig. 8). For all samples, with the increase of preparation temperature from 350 to 750 °C, the HDS rate decreases considerably, but unevenly. Low temperature IF and non-IF preparations have comparable HDS activity but with the increase of treatment temperature their catalytic performance diverges. The smaller is the IF particle size, the higher is the value of activity retained after treatment at 750 °C (HDS₇₅₀), as depicted in Fig. 8a. For the low preparation temperatures the amount of edges in both IF and non-IF MoS₂ is similar and high, so the overall HDS activity contains a major contribution from the edges. For high preparation temperatures the edges progressively disappear, whereas the curvature – generated sites remain on the surface (TPR section, Fig. 5).

The HDS₇₅₀ value seems to be diagnostic of the thermally stable curvature-related sites. Indeed, the HDS₇₅₀ value is weakly correlated with the amount of residual edges (Fig. 8b). On the other hand HDS₇₅₀ changes with the particle size more rapidly than the specific surface area or the R⁻¹ value. The HDS₇₅₀ vs. size changes approximately as R⁻² (Fig. 8b). Such dependence allows a simple physical interpretation. Both the specific surface area and the curvature change as R⁻¹. The HDS₇₅₀ is proportional to the product of surface area and the concentration of curvature-generated sites, so it changes as R⁻².

A surprisingly good correlation was observed between the TPR-estimated amount of curvature defects and the HDS₇₅₀ activity (Fig. S11a). The plot of HDS₇₅₀ vs. the intensity of Raman LA(M) band for the solids treated at 750 °C departs farther from linearity but a strong positive correlation is still obvious (Fig. S11b). Using the TPR value as an estimate of the number of active sites we obtained a specific frequency of $210 \pm 40 \times 10^{-5} \text{ s}^{-1}$ (number of thiophene molecules converted on a defect site at 300 °C). This value is much higher than usually presented in the literature for non-promoted MoS₂ catalysts. Indeed, usually pseudo-TOF is reported, with the frequency calculated per one metallic atom [66], or per edge site [67], both values being certainly

underestimated. As far as comparison is possible, the TOF calculated here is 2–3 times higher than thiophene HDS TOF on the non-promoted MoS₂ active sites calculated per a CO adsorption site (extrapolated to the same temperatures) [68]. The direct desulfurization (DDS) vs. hydrogenation (HYD) selectivity can be accessed from the distribution of thiophene conversion products at isoconversion [31,32]. The selectivity to butane decreases with the preparation temperature, independently on the IF-MoS₂ size (Fig. S12), indicating that curvature relative sites have a pronounced DDS character.

4. Conclusion

A new synthetic strategy has been used in this work to obtain size-tuned hollow sulfide particles of IF-MoS₂ from the AMoO₄ Scheelites (A = Ca, Sr, Ba). Beside individual IF-MoS₂ reported in this paper, synthesis of doped MoS₂ and mixed sulfides is possible using the same approach and the corresponding studies are underway.

Extended series of IF-MoS₂ materials with independently controlled particle size and slabs defectness allowed unraveling the contributions of slabs edges and curved (broken) basal planes to the catalytic activity. In step with the removal of the edge sites, the non-IF (ATM-derived MoS₂) sulfide materials lose their activity in both electrocatalytic HER and thiophene HDS. In contrast, under the same high-temperature conditions the IF-MoS₂ solids remain catalytically active due to thermally stable non-edge active sites. The magnitude of this effect depends on the particle size: smaller particles show higher specific curvature-related activity in both HER and HDS. In several previous works the basal planes curvature was supposed to play an important role in the hydrotreating [31,69]. However as no series of materials with controllable planes curvature was available, only hypotheses could be stated. Here for the first time the effect is systematically evidenced.

Defect-rich MoS₂ structures can be prepared using versatile chemical methods [70]. However in the flat 2D materials such defects can be easily annealed at elevated temperatures or during a long-time utilization. As with spherical IF-MoS₂ particles, they contain topologically irreducible defects which persist even after long-time annealing. Indeed, a sphere cannot be flattened on a plane without being torn apart (a well known problem in cartography). Therefore a spherical particle composed by 2D layers of sulfide must contain defects.

Further work should be aimed on both fundamental issues and applications. On the fundamental side, the properties of uniformly curved vs. broken slabs are yet to be understood. The effects of curvature as observed might provide new insights into the understanding of the effect of support in sulfide catalysts. Indeed, for chemically similar supports, one with higher curvature of particles might have an advantage over a less curved counterpart. This obvious consequence of the curvature effect was previously overlooked in the support effect studies.

On the applied side, promoted systems are to be investigated for HDS and other catalytic reactions. Thus, Co – promoted sites on the basal MoS₂ planes were recently reported to be active in hydrodeoxygenation [71]. The IF sulfides seem to be promising hosts for such new sites. Thermally stable and highly active catalysts containing sulfide layers rolled around small and rigid spherical support particles might be eminently interesting in relatively high-temperature applications, such as hydrotreating of heavy residues.

Acknowledgements

The author thanks Laurence Massin and Yoann Isaac (both IRCELYON) for performing XPS and XRD measurements, respectively.

Appendix A. Supplementary data

Supplementary data associated with this article can be found, in the online version, at <https://doi.org/10.1016/j.apcatb.2017.12.012>.

References

- [1] H. Topsøe, Appl. Catal. A: Gen. 322 (2007) 3–8.
- [2] L. van Haandel, G.M. Bremmer, E.J.M. Hensen, T.h. Weber, J. Catal. 351 (2017) 95–106.
- [3] M. Chhowalla, G.A. Amaralunga, Nature 407 (2000) 164–167.
- [4] M. Acerce, D. Voiry, M. Chhowalla, Nat. Nanotechnol. 10 (2015) 313–318.
- [5] Z.B. Lei, W.S. You, M.Y. Liu, G.H. Zhou, T. Takata, M. Hara, K. Domen, C. Li, Chem. Commun. (2003) 2142–2143.
- [6] L. Ye, C. Wu, W. Guo, Y. Xie, Chem. Commun. (2006) 4738–4740.
- [7] R. Huirache-Acuña, B. Pawelec, E.M. Rivera-Muñoz, R. Gui-López, J.L.G. Fierro, Fuel 198 (2017) 145–158.
- [8] C. Thomazeau, C. Geantet, M. Lacroix, M. Danot, V. Harlé, P. Raybaud, Appl. Catal. A Gen. 322 (2007) 92–97.
- [9] Z.Z. Wu, B.Z. Fang, A. Bonakdarpoor, A.K. Sun, D.P. Wilkinson, D.Z. Wang, Appl. Catal. B: Environ. 125 (2012) 59–66.
- [10] B. Lassalle-Kaiser, D. Merki, H. Vrubel, S. Gul, V.K. Yachandra, X.L. Hu, J. Yano, J. Am. Chem. Soc. 137 (2015) 314–321.
- [11] T.F. Jaramillo, K.P. Jorgenson, J. Bonde, J.H. Nielsen, S. Horch, I. Chorkendorff, Science 317 (2007) 100–102.
- [12] B. Hinnemann, P.G. Moses, J. Bonde, K.P. Jørgensen, J.H. Nielsen, S. Horch, I. Chorkendorff, J.K. Nørskov, J. Am. Chem. Soc. 127 (2005) 5308–5309.
- [13] J. Benson, M. Li, S. Wang, P. Wang, P. Papakonstantinou, ACS Appl. Mater. Interf. 7 (2015) 14113–14122.
- [14] J. Kibsgaard, Z. Chen, B.N. Reinecke, T.F. Jaramillo, Nat. Mater. 11 (2012) 963–969.
- [15] M.A. Lukowski, A.S. Daniel, C.R. English, F. Meng, A. Forticaux, R.J. Hamers, S. Jin, Energy Environ. Sci. 7 (2014) 2608–2613.
- [16] J. Zhang, Q. Wang, L.H. Wang, X. Li, W. Huang, Nanoscale 7 (2015) 10391–10397.
- [17] T. Wang, D. Gao, J. Zhuo, Z. Zhu, P. Papakonstantinou, Y. Li, M. Li, Chem. Eur. J. 19 (2013) 11939–11948.
- [18] D. Voiry, M. Salehi, R. Silva, T. Fujita, M. Chen, T. Asefa, V.B. Shenoy, G. Eda, M. Eda, Nano Lett. 13 (2013) 6222–6227.
- [19] D. Voiry, R. Fullon, J. Yang, C. de Carvalho Castro e Silva, R. Kappera, I. Bozkurt, M.J. Kaplan, G. Batson, A.D. Gupta, L. Mohite, D. Dong, V.B. Er Shenoy, T. Asefa, M. Chhowalla, Nat. Mater. 15 (2016) 1003–1009.
- [20] K. He, C. Poole, K.F. Mak, J. Shan, Nano Lett. 13 (2013) 2931–2936.
- [21] H. Shi, H. Pan, Y.W. Zhang, B.I. Yakobson, Phys. Rev. B 87 (2013) 155304.
- [22] S. Bertolazzi, J. Brivio, A. Kis, ACS Nano 5 (2011) 9703–9709.
- [23] Y. Kim, A.P. Tiwari, O. Prakash, H. Lee, ChemPlusChem 82 (2017) 785–791.
- [24] R. Tenne, Prog. Inorg. Chem. 50 (2004) 269–315.
- [25] Y. Feldman, E. Wasserman, D.J. Srolovitz, R. Tenne, Science 267 (1995) 222–225.
- [26] I. Wiesel, H. Arbel, A. Albu-Yaron, R. Popovitz-Biro, J.M. Gordon, D. Feuermann, R. Tenne, Nano Res. 2 (2009) 416–424.
- [27] D.M.D.J. Singh, T. Pradeep, J. Bhattacharjee, U.V. Waghmare, J. Phys. Chem. A 109 (2005) 7339–7342.
- [28] J. Etzkorn, H.A. Therese, F. Rocker, N. Zink, U. Kolb, W. Tremel, Adv. Mater. 17 (2005) 2372–2375.
- [29] X. Zuo, K. Chang, J. Zhao, Z. Xie, H. Tang, B. Li, Z. Chang, J. Mater. Chem. A 4 (2016) 51–58.
- [30] Y.Q. Zhu, T. Sekine, Y.H. Li, M.W. Fay, Y.M. Zhao, C.H. Patrick Poa, R. Tenne, J. Am. Chem. Soc. 127 (2005) 16263–16272.
- [31] A. Nogueira, R. Znaiguiua, D. Uzio, P. Afanasiev, G. Berhault, Appl. Catal. A: Gen. 429 (2012) 92–105.
- [32] P. Afanasiev, J. Catal. 269 (2010) 269–280.
- [33] P. Afanasiev, J. Solid State Chem. 229 (2015) 112–123.
- [34] P. Afanasiev, Catal. Today 250 (2015) 134–144.
- [35] I.S. Pap, G. Mink, A. Auroux, E. Karmazsin, J. Therm. Anal. 44 (1995) 847–854.
- [36] I.S. Pap, G. Mink, T. Székely, J. Therm. Anal. 36 (1990) 1765–1774.
- [37] A. Yella, M. Panthöfer, M. Kappl, W. Tremel, Angew. Chem. Int. Ed. 49 (2010) 2575–2580.
- [38] J.C. Sczancoski, L.S. Cavalcante, M.R. Joya, J.A. Varela, P.S. Pizani, E. Longo, Chem. Eng. J. 140 (2008) 632–637.
- [39] Y.H. Shen, W. Li, T.H. Li, Mater. Lett. 65 (2011) 2956–2958.
- [40] T. Thongtem, A. Phuruangrat, S. Thongtem, Mater. Lett. 62 (2008) 454–457.
- [41] F. Hoshyargar, T.P. Corrales, R. Branscheid, U. Kolb, M. Kappl, M. Panthöfer, W. Panthöfer, Dalton Trans. 42 (2013) 14568–14575.
- [42] N. Zink, H.A. Therese, J. Pansiot, A. Yella, F. Banhart, W. Tremel, Chem. Mater. 20 (2008) 65–71.
- [43] D. Vollath, D.V. Szabó, Mater. Lett. 35 (1998) 236–244.
- [44] S. Eijssbouts, X. Li, J. Juan-Alcaniz, L.C.A. van den Oetelaar, J.A. Bergwerff, J. Loos, A. Carlsson, E.T.C. Carlsson, ACS Catal. 7 (2017) 4817–4821.
- [45] C. Lee, X. Wei, J.W. Kysar, J. Hone, Science 321 (2008) 385–388.
- [46] S. Najmaei, Z. Liu, W. Zhou, X. Zou, G. Shi, S. Lei, B.I. Yakobson, J.C. Idrobo, P.M. Ajayan, J. Lou, Nat. Mater. 12 (2013) 754–759.
- [47] W. Zhou, X. Zou, S. Najmaei, Z. Liu, Y. Shi, J. Kong, J. Lou, P.M. Ajayan, B.I. Yakobson, J.C. Idrobo, Nano Lett. 13 (2013) 2615–2622.
- [48] N. Gao, Y. Guo, S. Zhou, Y. Bai, J. Zhao, J. Phys. Chem. C 121 (2017) 12261–12269.
- [49] X. Zhang, X.F. Qiao, W. Shi, J.B. Wu, D.S. Jiang, P.H. Tan, Chem. Soc. Rev. 44 (2015) (2757–2778).
- [50] H. Li, Q. Zhang, C.C.R. Yap, B.K. Tay, T.H.T. Edwin, A. Olivier, D. Baillargeat, Adv. Funct. Mater. 22 (2012) 1385–1390.
- [51] E. Blanco, P. Afanasiev, G. Berhault, D. Uzio, S. Loridant, C.R. Chim. 19 (2016) 1310–1314.
- [52] M. Cardona, M. Cardona, G. Güntherodt (Eds.), Light Scattering in Solids II, Springer-Verlag, Berlin, 1983, p. 19.
- [53] S. Mignuzzi, A.J. Pollard, N. Bonini, B. Brennan, I.S. Gilmore, M.A. Pimenta, D. Richards, D. Roy, Phys. Rev. B 91 (2015) 195411.
- [54] B. Chakraborty, H.S.S. Ramakrishna Matte, A.K. Sood, C.N.R. Rao, J. Raman Spectrosc. 44 (2013) 92–96.
- [55] M. Ye, D. Winslow, D. Zhang, R. Pandey, Y.K. Yap, Photonics 2 (2015) 288–307.
- [56] P. Afanasiev, Appl. Catal. A: Gen. 303 (2006) 110–115.
- [57] B. Baubet, E. Devers, A. Hugon, E. Leclerc, P. Afanasiev, Appl. Catal. A: Gen. 487 (2014) 72–81.
- [58] S. Sobczynski, J. Catal. 131 (1991) 156–166.
- [59] M. Chhetri, U. Gupta, L. Yadgarov, R. Rosentsveig, R. Tenne, C.N.R. Rao, ChemElectroChem 3 (2016) 1937–1943.
- [60] M. Chhetri, U. Gupta, L. Yadgarov, R. Rosentsveig, R. Tenne, C.N.R. Rao, Dalton Trans. 44 (2015) 16399–16404.
- [61] L. Yadgarov, D.G. Stroppa, R. Rosentsveig, R. Ron, A.N. Enyashin, L. Houben, R. Tenne, Z. Anorg. Allg. Chem. 638 (2012) 2610–2616.
- [62] Y.W. Tan, P. Liu, L.Y. Chen, W.T. Cong, Y. Ito, J.H. Han, X.W. Guo, Z. Tang, T. Fujita, A. Hirata, M.W. Chen, Adv. Mater. 26 (2014) 8023–8028.
- [63] A.N. Enyashin, S. Gemming, M. Bar-Sadan, R. Popovitz-Biro, S.Y. Hong, Y. Prior, R. Tenne, G. Seifert, Angew. Chem. Int. Ed. 46 (2007) 623–627.
- [64] E.J.M. Hensen, H.J.A. Brans, Lardinois G.M.H.J., V.H.J. de Beer, J.A.R. van Veen, R.A. van Santen, J. Catal. 192 (2000) 98–107.
- [65] Z. Vít, D. Gulková, L. Kaluža, M. Zdražil, J. Catal. 232 (2005) 447–455.
- [66] Y.E. Licea, R. Grau-Crespo, L.A. Palacio, A.C. Faro Jr., Catal. Today 292 (2017) 84–96.
- [67] P.A. Nikulshin, V.A. Salnikov, A.V. Mozhaev, P.P. Minaev, V.M. Kogan, A.A. Pimerzin, J. Catal. 309 (2014) 386–396.
- [68] C. Dujardin, M.A. Lélias, J. van Gestel, A. Travert, J.C. Duchet, F. Maugé, Appl. Catal. A: Gen. 322 (2007) 46–57.
- [69] E. Blanco, D. Uzio, G. Berhault, P. Afanasiev, J. Mater. Chem. A 220 (2014) 159–167.
- [70] J. Xie, H. Zhang, S. Li, R. Wang, X. Sun, M. Zhou, J. Zhou, X.W. Lou, Y. Xie, Adv. Mater. 25 (2013) 5807–5813.
- [71] G. Liu, A.W. Robertson, M.M.J. Li, W.C.H. Kuo, M.T. Darby, M.H. Muhieddine, Y.C. Lin, K. Suenaga, M. Stamatakis, J.H. Warner, S.C.E. Tsang, Nat. Chem. (2017), <http://dx.doi.org/10.1038/nchem.2740> (advance online publication.).